NUMERICAL STUDY OF TWO-DIMENSIONAL SOLID-GAS COMBUSTION THROUGH GRANULATED PROPELLANTS

Tony W. H. Sheu and Shi-Min Lee
Institute of Naval Architecture and Ocean Engineering, National Taiwan University, Taipei, Taiwan, Republic of China

In this paper, we deal with the governing equations of solid-gas two-phase fluid flow and transient combustion processes of granular propellants taking place in a gun chamber with a mobile projectile. We resort to a two-phase fluid dynamics model to model the solid-gas flow field. Due to the projectile motion, it is necessary to make the transformation from the coordinate parallel to the projectile motion to a new coordinate that remains invariant with time. Two sets of transformed basic equations for each phase are analyzed numerically, together with the constitutive equations for the intergranular stress, interphase drag, interphase heat transfer, diffusivity coefficients, and burning rate. In addition, an ignition criterion for the propellant grains must be given. The Noble-Abel equation of state was used for the gas phase in the present analysis. A finite volume method was employed to discretize the basic equations for both the compressible gas phase and propellant solid phase. The derived algebraic equations in a staggered grid system, by using an upwind scheme to approximate total fluxes, were solved iteratively by the newly proposed SIMPLE-COM ***solution algorithm. In this study, we address the variations of flow structure and physical properties during the ballistic cycle.***

INTRODUCTION

Combustion of granular solid propellants in a gun propulsion system has been studied by several research groups in the past two decades [1]. By means of these ballistic analyses, we are able to understand more about the establishment of high thrust within an extremely short time interval. The major concerns in such solid-gas two-phase combustion are related to the ignition, flame propagation, propellant deflagration, and flow unsteadiness.

The physics taking place in a gun interior ballistic cycle has been well described by Kuo [1]. The chemical reaction following the ignition of nonpacked

Received 21 March 1994; accepted 7 July 1994.

This research was conducted under a contract from the National Science Council, grant no. 80-0210-D032-01. Thanks are expressed to H.-C. Cheng, director of the Ballistic Research Center of the Combined Service Force, and his colleagues, who made this study possible. The authors also acknowledge the valuable comments and criticisms offered by Professor K. Kuo and Yigor Yang at Pennsylvania State University during the course of this work.

Present address of Shi-Min Lee is Institute of Aeronautics Engineering, Tamkang University, Tamsui, Taipei, Taiwan, 25137, Republic of China.

Address correspondence to Tony W. H. Sheu, Institute of Naval Architecture and Ocean Engineering, Colloge of Engineering, National Taiwan University, 73 Chow-Shan Road, Taipei, Taiwan, Republic of China.

Numerical Heat Transfer, Part A, 27:395–415, 1995

1040–7782/95 $10.00 + .00

NOMENCLATURE

a	coefficient in difference equation for variable ϕ	u_2, v_2	velocity components of propellant along x and y axes, respectively
b	source term in difference equation for variable ϕ	α_p	thermal diffusivity
c_p	specific heat	γ	weighting factor in Eq. (18)
D	diffusive flux on control volume surface	δ_p	length of physical domain
		$\Delta z, \Delta y, \delta z_e,$ δy_e, etc.	distances indicated in Figure 1
F	convective flux on control volume surface	μ	viscosity
h	gas phase static entropy	ρ	density
H_{comb}	chemical energy	τ	intergranular stress
K	thermal conductivity	ϕ	dependent variables
p	pressure		
Pe	Péclet number		
r	specific heat ratio	**Subscripts**	
R	volume fraction		
S	source term in differential equation for variable ϕ	e, w, n, s	four surface nodes of control volume around P
t	time		
T	temperature	E, W, N, S	four nodes adjacent to P shown in Figure 1
u_1, v_1	velocity components of gas phase along x and y axes, respectively	P	control nodal point for a primitive variable, i.e., u, v, p, or h

solid propellants can be completed only within a few milliseconds in the gun barrel. The hot gases, released from the burned black powders in the center core igniter near the front end of the barrel, penetrate into the voids and lead to the ignition of solid granules by convective heating. Both granule compaction and rapid pressurization are then set up in the subsequent ballistic cycle. The ignition front is accelerated from a moderate to a higher pace due to the interior pressure buildup. These ignited propellants give off more hot gases and are pushed forward by the developed pressure gradient. More propellants are thus ignited. A shocklike steep pressure gradient is thus formed inside the combustion chamber, and the pressure behind the shock line is very high. The resulting accelerated gaseous products finally cause the projectile to move. The flame spreading and the possible shock-front formation in the porous propellant charges are certainly important in loading an appropriate amount of propellants for achieving the desired propulsion.

Experimental investigation of internal ballistic combustion processes is not only difficult and expensive to perform but is also subject to a high degree of uncertainty or inaccuracy. The advances in computer resources and computational techniques provide an alternative means to analyze such a complex solid-gas flow field. Numerical studies of combustion physics in a gun interior have been the subject of many investigations that began as early as the 1950's [2]. The first set of partial differential equations capable of depicting the interior ballistic physics was proposed by Baer [3]. Later in 1973, Kuo et al. [4] designed a fixed granular bed combustion model to simulate the flame spreading and combustion phenomena in the granular beds. Quasi-one-dimensional models of mobile granular bed combus-

tion have been proposed [5–8]. Extension to multidimensional analysis, which is the major aim of the present study, is the current research topic in the area of gun interior ballistics.

In simulating the complex physics in a gun interior full of ignitable granular propellants, the existing physical models can be classified mainly into the statistical model [9], the continuum-mechanics method [10], and the formal averaging method [11–13]. In most computer codes, they were developed with the underlying one-dimensional assumption. The major contributors are as follows: (1) MGBC code by Kuo and colleagues [5]; (2) CALSPAN code by Fisher and Graves [14]; (3) NOVA code by Gough [15], and (4) PHOENICS code by Markatos [16]. For the sake of sharply capturing any abrupt change taking place in the flow passage, a flux corrected transport (FCT) technique has been incorporated to the two-step Lax-Wendroff discretization scheme [17]. Extensions to multidimensional analyses have been accomplished more recently [18–21].

The objective of this study is to develop an interior ballistics code for predicting the pressure formation, flame spreading, and combustion of large solid-propellant grains in the gun cartridges. The mass, momentum, and energy fluxes are balanced over a control volume containing certain amounts of space-sharing interspersed continua. Two sets of equations for the solid and gas phases are coupled with an interaction drag, heat transfer to the propellant grains, and other correlations related to the combustion. The shares of gas and solid phases are commonly measured by the value of volume fraction.

BASIC EQUATIONS

We analyzed the transient combustion processes in a granular propellant bed numerically by solving two sets of individual equations for each phase. Both gas and solid phases were distributed dispersedly and coupled with the appropriate interaction relations. Each phase itself is a continuum. The commonly embedded lead-foil decoppering media for reducing the rate of copper buildup on the chamber surfaces were not considered here for the sake of simplicity. In addition, the solid propellants were not splintered during the burning processes. In each phase the resulting changes in mass, momenta, and energy can be represented by the following expressions on condition that the turbulence is not modeled for the time being. The volume-sharing principle is adopted and given by $R_1 + R_2 = 1$, where the void fraction for the gas is R_1 while the void fraction for the remaining solid phase is R_2.

Gas Phase: Set 1

$$\frac{\partial(\rho_1 R_1 \phi)}{\partial t} + \frac{\partial(\rho_1 R_1 u_1 \phi)}{\partial x} + \frac{\partial(\rho_1 R_1 v_1 \phi)}{\partial y}$$

$$= \frac{\partial}{\partial x}\left(\Gamma R_1 \frac{\partial \phi}{\partial x}\right) + \frac{\partial}{\partial y}\left(\Gamma R_1 \frac{\partial \phi}{\partial y}\right) + S \tag{1}$$

Table 1. Definitions of ϕ, Γ, and S in gas-phase equations

	ϕ	Γ	S
Continuity	1	0	$\dot{m}$
x Momentum	u_1	μ	$-R_1\frac{\partial P}{\partial x}+\frac{\mu}{3}\frac{\partial}{\partial x}\left[R_1\left(\frac{\partial u_1}{\partial x}+\frac{\partial v_1}{\partial y}\right)\right]-\frac{3R_2\dot{F}_x}{r_p}+u_2\dot{m}$
y Momentum	v_1	μ	$-R_1\frac{\partial P}{\partial y}+\frac{\mu}{3}\frac{\partial}{\partial y}\left[R_1\left(\frac{\partial u_1}{\partial x}+\frac{\partial v_1}{\partial y}\right)\right]-\frac{3R_2\dot{F}_y}{r_p}+v_2\dot{m}$
Energy	h	0	$\frac{\partial}{\partial x}\left[R_1K_1\left(\frac{\partial T_1}{\partial x}\right)\right]+\frac{\partial}{\partial y}\left[R_1K_1\left(\frac{\partial T_1}{\partial y}\right)\right]$ $+R_1\left(\frac{\partial P}{\partial t}+\frac{\partial(u_1P)}{\partial x}+\frac{\partial(v_1P)}{\partial y}-P\frac{\partial u_1}{\partial x}-P\frac{\partial v_1}{\partial y}\right)$ $+\dot{m}\{H_{comb}+0.5[(u_1-u_2)^2+(v_1-v_2)^2]\}$ $+3\frac{R_2}{r_p}(\mathbf{u}_1-\mathbf{u}_2)\cdot\mathbf{F}-3\frac{R_2}{r_p}\dot{Q}$

where ϕ is the dependent variable, Γ is the diffusivity, and S the source term given in Table 1. Heat transfer rate $\dot{Q}$ will be defined later in this section.

Solid phase: Set 1

$$\frac{\partial(\rho_2R_2\phi)}{\partial t}+\frac{\partial(\rho_2R_2u_2\phi)}{\partial x}+\frac{\partial(\rho_2R_2v_2\phi)}{\partial y}$$
$$=\frac{\partial}{\partial x}\left(\Gamma R_2\frac{\partial\phi}{\partial x}\right)+\frac{\partial}{\partial y}\left(\Gamma R_2\frac{\partial\phi}{\partial y}\right)+S \tag{2}$$

where the definitions of ϕ, Γ, and S values are given in Table 2. Hereinafter we refer to P as pressure.

The theoretical modeling for such a flow system has undergone a number of major advances over the past four decades. It began with the lumped parameter analysis [22] and evolved to the models for fixed [4] and mobile granular bed combustion [5–7]. In order to simulate the combustion processes of mobile granular propellants, it is necessary to make the transformation from one coordinate

Table 2. Definitions of ϕ, Γ, and S in solid-phase equations

	ϕ	Γ	S
x Momentum	u	0	$-R\frac{\partial P}{\partial x}-\frac{\partial}{\partial x}(R\tau)+\frac{3R_2\dot{F}_x}{r_p}-u\dot{m}$
y Momentum	v	0	$-R\frac{\partial P}{\partial y}-\frac{\partial}{\partial y}(R\tau)+\frac{3R_2\dot{F}_y}{r_p}-v\dot{m}$
particle radius	r_p	$\mu/0.9$	$-4R\rho\dot{d}$

system (x, y) to another (z, y) that remains invariant with time. The relation between two such coordinates is

$$z = \frac{x}{\delta_P} \tag{3}$$

where $\delta_P(t)$ is the length of the physical domain. Through the use of the above transformation, we can distribute the expansion grids to the variable physical domain. The computations consequently can be carried out on a fixed computational domain when solving a truly domain-varying problem. The flow is characterized by the following Navier-Stokes equations written in the transformed coordinates.

Gas phase: Set 2

$$\frac{1}{\delta_P}\frac{d(\rho_1\delta_P R_1\phi)}{dt} + \frac{1}{\delta_P}\frac{\partial(\rho_1 R_1\bar{u}_1\phi)}{\partial z} + \frac{\partial(\rho_1 R_1 v_1\phi)}{\partial y}$$

$$= \frac{1}{\delta_P}\frac{\partial}{\partial z}\left(\frac{1}{\delta_P}\Gamma R_1\frac{\partial\phi}{\partial z}\right) + \frac{\partial}{\partial y}\left(\Gamma R_1\frac{\partial\phi}{\partial y}\right) + S \tag{4}$$

where $\bar{u}_i = u_i - z(\partial\delta_P/\partial t)$ $(i = 1, 2)$ and the expressions for ϕ, Γ, and S are given in Table 3.

Table 3. Definitions of ϕ, Γ, and S for gas-phase equations in moving coordinates

	ϕ	Γ	S
Continuity	1	0	$\dot{m}$
z Momentum	u_1	μ	$-\frac{R_1}{\delta_P}\frac{\partial P}{\partial z} + \frac{\mu}{3\delta_P}\frac{\partial}{\partial z}\left[R_1\left(\frac{1}{\delta_P}\frac{\partial u_1}{\partial z} + \frac{\partial v_1}{\partial y}\right)\right] - \frac{3R_2\dot{F}_x}{r_P} + u_2\dot{m}$
y Momentum	v_1	μ	$-R_1\frac{\partial P}{\partial y} + \frac{\mu}{3}\frac{\partial}{\partial y}\left[R_1\left(\frac{1}{\delta_P}\frac{\partial u_1}{\partial x} + \frac{\partial v_1}{\partial y}\right)\right] - \frac{3R_2\dot{F}_y}{r_P} + v_2\dot{m}$
Energy	h	0	$\frac{1}{\delta_P}\frac{\partial}{\partial z}\left[R_1K_1\left(\frac{1}{\delta_P}\frac{\partial T_1}{\partial z}\right)\right] + \frac{\partial}{\partial y}\left[R_1K_1\left(\frac{\partial T_1}{\partial y}\right)\right]$ $+R_1\left(\frac{\partial P}{\partial t} + \frac{1}{\delta_P}\frac{\partial(u_1P)}{\partial z} + \frac{\partial(v_1P)}{\partial y} - P\frac{1}{\delta_P}\frac{\partial u_1}{\partial z} - P\frac{\partial v_1}{\partial y}\right)$ $+\dot{m}\{H_{comb} + 0.5[(u_1 - u_2)^2 + (v_1 - v_2)^2]\}$ $+3\frac{R_2}{r_P}(\mathbf{u}_1 - \mathbf{u}_2)\cdot\mathbf{F} - 3\frac{R_2}{r_P}\dot{Q}$

Solid phase: Set 2

$$\frac{1}{\delta_P}\frac{d(\rho_2\delta_P R_2\phi)}{dt} + \frac{1}{\delta_P}\frac{\partial(\rho_2 R_2 u_2\phi)}{\partial z} + \frac{\partial(\rho_2 R_2 v_2\phi)}{\partial y}$$

$$= \frac{1}{\delta_P}\frac{\partial}{\partial z}\left(\frac{1}{\delta_P}\Gamma R_2\frac{\partial\phi}{\partial z}\right) + \frac{\partial}{\partial y}\left(\Gamma R_2\frac{\partial\phi}{\partial y}\right) + S \tag{5}$$

where the meanings of ϕ, Γ, and S are given in Table 4.

$$\frac{1}{\delta_P}\frac{d(\rho_2\delta_P\phi)}{dt} + \frac{1}{\delta_P}\frac{\partial(\rho_2\bar{u}_2\phi)}{\partial z} + \frac{\partial(\rho_2 v_2\phi)}{\partial y} = S \tag{6}$$

As for the continuity, we designate $\phi = R_2$ and $\Gamma = -\dot{m}$.

CONSTITUTIVE EQUATIONS

A number of constitutive equations are indispensable in order to close the problem. The nonideal Noble-Abel equation of state [1] has been known to be able to represent the gas phase present in gun interior ballistics,

$$P = \frac{\rho_1\bar{R}T}{(1 - b\rho_1)} \tag{7}$$

where $\bar{R}$ is the universal gas constant and b is the so-called co-volume.

The employed auxiliary constitutive equations for the closure of Eqs. (4)–(6) are also described as follows.

Intergranular Stress

An intergranular stress will arise in a partially packed barrel in order to keep particles apart. It implies that the solid propellants cannot occupy the whole space.

Table 4. Definitions of ϕ, Γ, and S for solid-phase equations in moving coordinates

	ϕ	Γ	S
x Momentum	u_2	0	$-R_2\frac{1}{\delta_P}\frac{\partial P}{\partial z} - \frac{1}{\delta_P}\frac{\partial}{\partial z}(R_2\tau) + \frac{3R_2\dot{F}x}{r_P} - u_2\dot{m}$
y Momentum	v_2	0	$-R_2\frac{\partial P}{\partial y} - \frac{\partial}{\partial y}(R_2\tau) + \frac{3R_2\dot{F}y}{r_P} - v_2\dot{m}$
Energy	r_P	$\mu/0.9$	$-4R_2\rho_2\dot{d}$

This isotropic normal stress τ in the solid phase takes the following form [16] and can only affect the granules:

$$\begin{aligned} \tau &= 0 && R_1 > R_0 \\ \tau &= K(R_2 - R_0) && R_1 \le R_0 \end{aligned} \tag{8}$$

where $K = 1.76 \times 10^8$ N/m^2. No direct contact between particles is assumed, as the value of porosity exceeds the critical value of R_0 ($R_0 = 0.5$ in the present analysis).

Interphase Drag

For the investigated packed bed, the average steady state interphase drag **D** appearing in the momentum equations is represented empirically by the following correlation:

$$\mathbf{D} = R_2 \frac{S}{V} \mathbf{F} \tag{9}$$

where $S = 4\pi r_P^2$ and $V = 4/3\pi r_P^3$ represent surface area and volume of a spherical particle, respectively. The interphase drag per unit area of solid phase is obtained from Ergun's equation as given by Corner [22]:

$$\mathbf{F} = \frac{\rho_1(\mathbf{u}_1 - \mathbf{u}_2)|\mathbf{u}_1 - \mathbf{u}_2|}{6} \hat{f} \tag{10a}$$

where

$$\begin{aligned} \hat{f} &= 1.75 && R_1 \le R_0 \\ \hat{f} &= 1.75\left(\frac{R_0}{R_1} \times \frac{R_2}{(1 - R_0)}\right)^{0.45} && R_0 \le R_1 \le R_l \\ \hat{f} &= 0.38 && R_l < R_1 \le 1 \end{aligned} \tag{10b}$$

and

$$R_l = \frac{1}{[1 + 0.02(1 - R_0/R_0)]} \tag{10c}$$

Particle Burning Rate

In analyzing systems of Eqs. (4) and (5), we have to define the rate of burned propellant $\dot{m}$, given by

$$\dot{m} = \frac{3R_2 \rho_2}{r_P} \dot{d} \tag{11}$$

where r_P is the time-varying radius of a propellant grain. The rate of surface regression for a particle was simplified as follows by the pressure-dependent burning law given in Ref. [19]:

$$\dot{d} = BP^n \tag{12}$$

Both proportionality constant B and the index of propellant burning rate in Eq. (12) should be specified empirically for the investigated propellants.

Gas-Solid Interphase Heat Transfer

The rate of heat transfer per unit time $\dot{Q}$ is the result of temperature differences across the granule surface. For both packed and fluidized beds, we model this rate using the following equation [19]:

$$\dot{Q} = H_c(T_1 - T_{2s}) \tag{13}$$

The proportional constant H_c in Eq. (13) is the total heat transfer coefficient across a phase boundary, defined by

$$H_c = \frac{K_1}{2r_P}\mathrm{Nu}_P \tag{14}$$

where the Nusselt number Nu_P and the Reynolds number Re_P are given by

$$\mathrm{Nu}_P = 2 + 0.4\,\mathrm{Re}_P^{2/3}\,\mathrm{Pr}^{1/3} \qquad \mathrm{Re}_P = \frac{2r_P\rho_1|\mathbf{u}_1 - \mathbf{u}_2|}{\mu}$$

Molecular Transport Properties

We used Sutherland's law [19] for the time being to compute the molecular viscosity μ and thermal conductivity k. Both are only functions of temperature:

$$\mu = \frac{C_1T^{3/2}}{C_2 + T} \tag{15}$$

$$k = \frac{C_3T^{3/2}}{C_4 + T} = \frac{c_p}{\mathrm{Pr}}\mu \tag{16}$$

where the value of specific heat c_p is given in Table 5, and

$$C_1 = 0.7535 \times 10^{-6}\,\mathrm{lbm/ft} - s - \sqrt{R} \qquad C_2 = 262.5R$$

$$C_3 = 0.291 \times 10^{-6}\,\mathrm{Btu/ft} - s - R^{3/2}$$

$$C_4 = 170.1R \qquad \mathrm{Pr} = \frac{4\gamma}{9\gamma - 5} \qquad \gamma = 1.27$$

NUMERICAL DISCRETIZATION

The above Eqs. (4)–(6) will be discretized by a finite volume method for both compressible gas and incompressible solid phases. When simulating combustion processes during the ballistic cycle, it is common to encounter oscillatory pressure wiggles in the vicinity of high gradients. One can suppress such numerical oscillations, for example, by correcting the erroneous fluxes computed from the second-order Lax-Wendroff scheme [17]. Since the concept underlying the total variation of diminishment (TVD) [23] does not accommodate two-dimensional analysis, the present study does not consider any high-resolution discontinuity capturing scheme. Given this, we employed a power law scheme [24] to approximate the flux terms, so that the oscillatory solutions will not appear.

$$a_P \phi_P = a_E \phi_E + a_w \phi_w + a_N \phi_N + a_S \phi_S + b \tag{17}$$

where

$$a_E = D_e \max\left[0, (1 - 0.1|P_e|)^5\right] + \max(-F_e, 0)$$

$$a_W = D_w \max\left[0, (1 - 0.1|P_w|)^5\right] + \max(-F_w, 0)$$

$$a_N = D_n \max\left[0, (1 - 0.1|P_n|)^5\right] + \max(-F_n, 0)$$

$$a_S = D_s \max\left[0, (1 - 0.1|P_s|)^5\right] + \max(-F_s, 0)$$

$$a_P^0 = \rho_P^0 R_P^0 \, \Delta z \, \Delta y / \Delta t$$

$$a_P = a_E + a_W + a_N + a_S + a_P^0 + S_m \, \Delta z \, \Delta y$$

$$b = S \, \Delta z \, \Delta y + a_P^0 \phi_P^0$$

and

$$D_e = \frac{\Gamma_e R_e}{\delta_P^2} \frac{\Delta y}{(\delta z)_e} \qquad D_w = \frac{\Gamma_w R_w}{\delta_P^2} \frac{\Delta y}{(\delta z)_w}$$

$$D_n = \frac{\Gamma_n R_n}{\delta_P^2} \frac{\Delta y}{(\delta z)_n} \qquad D_s = \frac{\Gamma_s R_s}{\delta_P^2} \frac{\Delta y}{(\delta z)_s}$$

$$F_e = (\rho R \bar{U})_e \frac{\Delta y}{\delta_P} \qquad F_w = (\rho R \bar{U})_w \frac{\Delta y}{\delta_P} \qquad F_n = (\rho R V)_n \, \Delta z \qquad F_s = (\rho R V)_s \, \Delta z$$

$$P_e = \frac{F_e}{D_e} \qquad P_w = \frac{F_w}{D_w} \qquad P_n = \frac{F_n}{D_n} \qquad P_s = \frac{F_s}{D_s}$$

$$\rho = (\rho_1, \rho_2) \qquad \bar{U} = (\bar{u}_1, \bar{u}_2) \qquad V = (v_1, v_2)$$

$$R = R(R_1, R_2) \qquad S_m = (\dot{m}, -\dot{m})$$

The notation (,) represents the values of (gas phase, solid phase).

The algebraic equations were discretized in a staggered grid system, shown in Figure 1, and were solved iteratively by the pressure-based compressible solution algorithm [25]. The calculation starts with the given initial condition. Within each time interval, we compute the time-accurate solutions iteratively from the guessed pressure field p^*. The corresponding velocities u_1^*, v_1^* were computed from the x and y gas momentum equations, respectively. The equation of state was used to compute the density ρ_1. With the computed velocity field u_1, the gas continuity equation is not necessarily satisfied, so that the pressure field should be corrected. The resulting Poisson equation for the pressure correction can be similarly discretized by a finite volume method:

$$a_P^\rho p'_P = a_E^\rho p'_E + a_W^\rho p'_W + a_N^\rho p'_N + a_S^\rho p'_S + b^\rho \tag{18}$$

where

$$a_E^\rho = \left[\left(\frac{1}{2} + \gamma_e\right)\rho_P^* + \left(\frac{1}{2} - \gamma_e\right)\rho_E^*\right] R_e^* d_e \frac{\Delta y}{\delta_P} - \left(\frac{1}{2} - \gamma_e\right) R_e^* \bar{u}_e C_E^\rho \frac{\Delta y}{\delta_P}$$

$$a_W^\rho = \left[\left(\frac{1}{2} + \gamma_w\right)\rho_W^* + \left(\frac{1}{2} - \gamma_w\right)\rho_P^*\right] R_w^* d_w \frac{\Delta y}{\delta_P} - \left(\frac{1}{2} + \gamma_w\right) R_w^* \bar{u}_w C_W^\rho \frac{\Delta y}{\delta_P}$$

$$a_N^\rho = \left[\left(\frac{1}{2} + \gamma_n\right)\rho_P^* + \left(\frac{1}{2} - \gamma_n\right)\rho_N^*\right] R_n^* d_n \Delta z - \left(\frac{1}{2} - \gamma_n\right) R_n^* v_n C_N^\rho \Delta z$$

$$a_S^\rho = \left[\left(\frac{1}{2} + \gamma_s\right)\rho_S^* + \left(\frac{1}{2} - \gamma_s\right)\rho_P^*\right] R_s^* d_s \Delta z - \left(\frac{1}{2} + \gamma_s\right) R_s^* v_s C_S^\rho \Delta z$$

$$a_P^\rho = a_E^\rho + a_W^\rho + a_N^\rho + a_S^\rho + R_P^* C_P^\rho \left(\frac{1}{\Delta t} + \frac{u_P}{\delta_P}\right) \Delta z \Delta y$$

$$+ \left[\left(\frac{1}{2} + \gamma_e\right) C_P^\rho + \left(\frac{1}{2} - \gamma_e\right) C_E^\rho\right] R_e^* \bar{u}_e^* \frac{\Delta y}{\delta_p}$$

$$- \left[\left(\frac{1}{2} + \gamma_w\right) C_W^\rho + \left(\frac{1}{2} - \gamma_w\right) C_P^\rho\right] R_w^* \bar{u}_w^* \frac{\Delta y}{\delta_P}$$

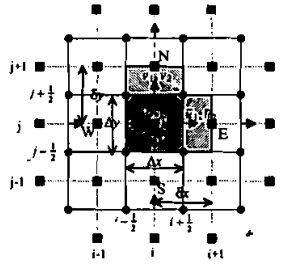

Figure 1. Staggered grid system.

$$+\left[\left(\frac{1}{2}+\gamma_n\right)C_P^{\rho}+\left(\frac{1}{2}-\gamma_n\right)C_N^{\rho}\right]R_n^* v_n^*\,\Delta z$$

$$-\left[\left(\frac{1}{2}+\gamma_s\right)C_S^{\rho}+\left(\frac{1}{2}-\gamma_s\right)C_P^{\rho}\right]R_s^* v_s^*\,\Delta z$$

$$b^{\rho}=(\rho_P^0-\rho_P^*)R_P^*\frac{\Delta z\,\Delta y}{\Delta t}-\frac{\rho_P^* R_P^* \bar{u}_P^*}{\delta_P}\Delta z\,\Delta y+\dot{m}\,\Delta z\,\Delta y$$

$$-\left[\left(\frac{1}{2}+\gamma_e\right)\rho_P^*+\left(\frac{1}{2}-\gamma_e\right)\rho_E^*\right]R_e^*\bar{u}_e^*\frac{\Delta y}{\delta_p}$$

$$+\left[\left(\frac{1}{2}+\gamma_w\right)\rho_W^*+\left(\frac{1}{2}-\gamma_w\right)\rho_P^*\right]R_w^*\bar{u}_w^*\frac{\Delta y}{\delta_P}$$

$$-\left[\left(\frac{1}{2}+\gamma_n\right)\rho_P^*+\left(\frac{1}{2}-\gamma_n\right)\rho_N^*\right]R_n^* v_n^*\,\Delta z$$

$$+\left[\left(\frac{1}{2}+\gamma_s\right)\rho_S^*+\left(\frac{1}{2}-\gamma_s\right)\rho_P^*\right]R_s^* v_s^*\,\Delta z$$

$$d_e=\frac{\Delta y}{a_e-\Sigma a_{nb}}\qquad d_w=\frac{\Delta y}{a_w-\Sigma a_{nb}}\qquad d_n=\frac{\Delta y}{a_n-\Sigma a_{nb}}\qquad d_s=\frac{\Delta z}{a_s-\Sigma a_{nb}}$$

The velocity components and density were then replaced in response to the change in pressure, as follows:

$$u_{le}=u_{le}^*+d_e(p'_P-p'_E) \tag{19a}$$

$$v_{ln}=v_{ln}^*+d_n(p'_P-p'_N) \tag{19b}$$

$$\rho_P=\rho_P^*+C_P^{\rho}p'_P \tag{19c}$$

The definitions of C_P^{ρ} can be found in Ref. [26].

By substituting the updated gas velocities, pressure, and density into the gas phase energy equation, one can calculate the gas temperature T_1. The particle velocities u_2 and v_2 can be computed directly from x and y solid phase momentum equations using the most updated data of the gas phase. The void fraction R_2 can then be computed from the continuity equation of the solid phase. The time-varying radius r_p of a particle is then ready to be computed. Repeat the preceeding computations by the updated pressure p^* until all the user-supplied convergence tolerances for gas velocities, pressure, gas temperature, propellant velocities, void fraction R_2, and particle radius r_p are reached. The computed time accurate solutions prior to the solid propellant being ignited are then used to

compute the temperature at the particle surface from the solid energy equation

$$\frac{1}{\alpha_P}\frac{\partial T_2}{\partial t} = \frac{\partial^2 T_2}{\partial r^2} + \frac{2}{r}\frac{\partial T_2}{\partial r}$$

The energy equation in a spherical coordinate system was discretized using the following forward-time and center-spaced scheme:

$$T_j = \frac{\alpha_P \Delta t}{(\Delta r_{j-1})^2}(T_{j-1}^n - 2T_j^n + T_{j+1}^n) + T_j^n \qquad j = 1,2,\ldots,k \tag{20}$$

The associated boundary conditions took the following form:

$$T_{k+1} = T_{k-1} \qquad r = 0$$

$$\frac{T_0 - T_2}{2\,\Delta r_1} = \frac{H_c}{K_2}(T_\infty - T_1) \qquad r = r_P$$

This completes the iterative solution processes for a time step Δt. The computed time accurate dependent variables will be used as the initial conditions if one wishes to continue the analysis before the investigated time of interest is reached.

The physical domain between the breech and projectile was first divided into N cells. In the course of pressurization, the physical domain will be expanded as the force acting on the projectile exceeds the spindle force. The total force F on the projectile base surface A_b can be obtained by integrating the differential force $dF = (p_b - p_{atm})A_b$ on the projectile surface, where p_b is the pressure acting on that surface. The length of the physical domain and the projectile velocity for the combustion analysis at the next time step can be computed respectively from

$$\delta_P = \delta_P^n + u_P^n \Delta t + \frac{1}{2}\frac{F}{2M_{\text{projectile}}}\Delta t^2 \tag{21}$$

$$u_P = u_P^n + \frac{F}{M_{\text{projectile}}}\Delta t \tag{22}$$

PROBLEM DESCRIPTION

The physical domain of the internal ballistic cycle to be simulated is illustrated in Figure 2. The main components in the investigated combustion system include the center core igniter, uniformly distributed spherical solid propellants, and a projectile. The base pad containing black powders is ignited at the center of the igniter tube. At one end of the chamber is the igniter assembly, and at the

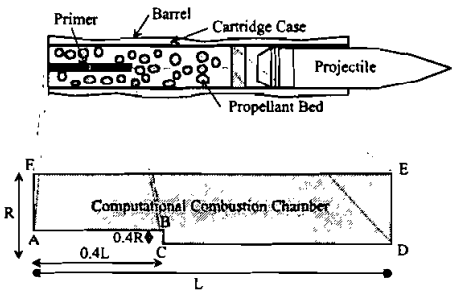

Figure 2. Computational domain of the internal ballistic cycle.

other end is the projectile, which is propelled forward as the given prescribed pressure is reached. Our aim is to simulate the truly transient combustion processes in a mobile system.

The charge was ignited by the ventilation of hot gases from a primer into a packed bed of solid propellant grains. The multiperforated propellant grains in the neighborhood of the primer were convectively heated by the hot gases. The representation of such an ignition train was based on the lumped conservation analysis. Ideally, the released chemical energy from the burned black powders is completely converted to the uniformly distributed hot gaseous streams. The ignited particles in turn produce hot gases and ignite more propellant grains, since the solid propellant has a higher burning rate. A bag of uniformly loaded propellants was investigated, and their physical properties are summarized in Table 5.

The initial void fraction of solid propellants inside the ballistic chamber is an important issue. Lower loading density may fail to deliver a force strong enough to propel the projectile to the desired distance. A tightly packed bed, on the other hand, may result in an incomplete combustion process. The present loading density is taken to be 0.5. The propellants begin being ignited as their surface temperature exceeds the ignition temperature $T_{ign} = 450°K$. For the sake of clarity, the investigated flow conditions were also tabulated in Table 5 for the initial size of solid propellants $r_p = 5 \times 10^{-4}$ m. The aspect ratio of igniter width is $0.4R$, and the chamber length is $L = 0.1$ m. The major computed results of interest include the axial distributions of pressure, porosity, density, and temperature at different stages in the course of projectile motion.

The analysis can be conducted only in a half chamber due to the geometric as well as physical symmetry. The boundary conditions are shown in Figure 2 and are summarized as follows:

For $\overline{AF}, \overline{EF}$

$$\frac{\partial P}{\partial n} = 0 \qquad \frac{\partial T_1}{\partial n} = 0 \qquad \frac{\partial \rho_1}{\partial n} = 0$$

$$\frac{\partial R_2}{\partial n} = 0 \qquad \frac{\partial r_P}{\partial n} = 0 \qquad u_1 = 0 \qquad u_2 = 0$$

$$v_1 = 0 \qquad v_2 = 0$$

Table 5. Test problem input conditions

	Property	Notation	Value
Gas phase	Density	ρ_1	1.2 kg/m^3
	Initial pressure	P_1	1.014×10^5 N/m^2
	Initial temperature	T_1	294 K
	Initial velocity	u_1, v_1	0
	Specific heat ratio	r	1.27
	Universal gas constant	$\bar{R}$	287 J/(kg K)
	Specific heat	c_P	2000 J/(kg K)
	Viscosity	μ	1.78×10^{-5} N s/m^2
	Thermal conductivity	K_1	0.045 (kg m)/(s^3 K)
	Prandtl number	Pr	0.79
	Co-volume	b	10^{-3} m^3/kg
Ignition	Mass inflow rate	$\dot{M}_{in}$	20 kg/s
	Period of ignition	t_{in}	5 ms
	Temperature	T_{in}	2000 K
Propellant	Density	ρ_2	1500 kg/m^3
	Initial temperature	T_2, T_{2s}	294 K
	Initial velocity	u_2, v_2	0
	Initial volume fraction	R_2	0.5
	Ignition temperature	T_{ing}	400 K
	Critical volume fraction	R_0	0.5
	Specific heat	c_P	2000 J/(kg K)
	Thermal conductivity	K_2	0.2(kg m)/(s^3 K)
	Thermal diffusivity	α_P	6.68×10^{-8} m^2/s
	Chemical energy	H_{comb}	4.0×10^6 J/kg
	Burning rate proportionality constant	B	0.25116 cm/s
	Burning rate index	n	0.6
	Intergranular stress proportionality constant	K	1.76×10^8 N/m^2
Projectile	Mass	$M_{projectile}$	4 kg
	Friction	Friction	10^6 N

For $\overline{DE}$

$$\frac{\partial P}{\partial n} = 0 \qquad \frac{\partial T_1}{\partial n} = 0 \qquad \frac{\partial \rho_1}{\partial n} = 0$$

$$\frac{\partial R_2}{\partial n} = 0 \qquad \frac{\partial r_P}{\partial n} = 0 \qquad u_1 = u_P \qquad \frac{\partial u_2}{\partial n} = 0$$

$$v_1 = 0 \qquad v_2 = 0$$

For $\overline{CD}$

$$\frac{\partial P}{\partial n} = 0 \qquad \frac{\partial T_1}{\partial n} = 0 \qquad \frac{\partial \rho_1}{\partial n} = 0$$

$$\frac{\partial R_2}{\partial n} = 0 \qquad \frac{\partial r_P}{\partial n} = 0 \qquad \frac{\partial u_1}{\partial n} = 0 \qquad \frac{\partial u_2}{\partial n} = 0$$

$$v_1 = 0 \qquad v_2 = 0$$

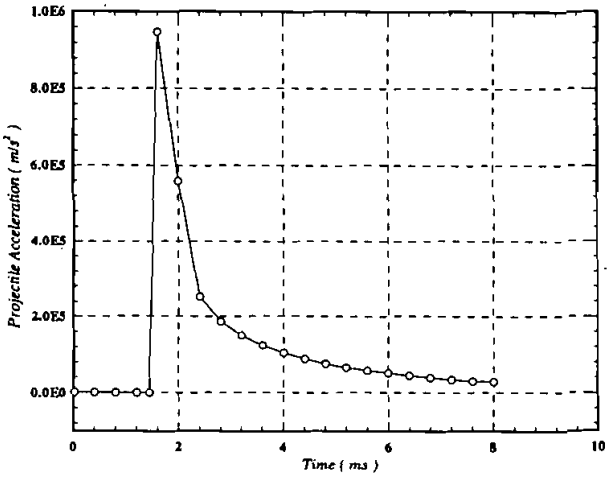

Figure 3. Computed projectile acceleration history.

COMPUTED SOLUTIONS

The kinematic process for the investigated two-phase mobile system can be best described by Figures 3 and 4, where the projectile acceleration and velocity histories are plotted. It is seen that the projectile starts moving at a time roughly equal to 2 ms and accelerates rapidly to a peak value of 9.48×10^5 m/s^2 at a time slightly less than 2 ms. The projectile acceleration then terminates in response to the decrease of the driving force at the projectile base, while its velocity continues to increase up to the value of 1200 m/s at time $t = 8$ ms.

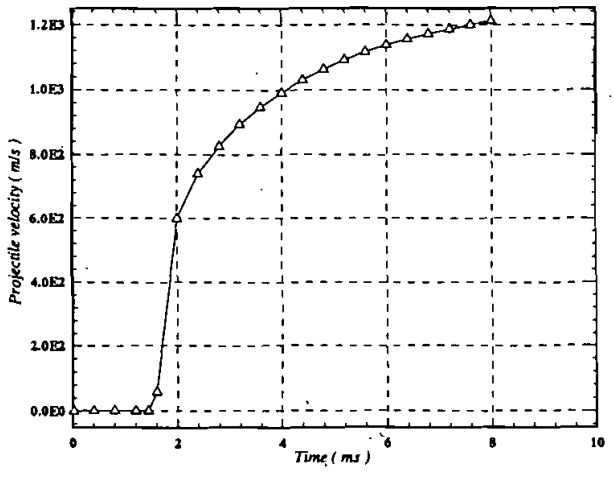

Figure 4. Computed projectile velocity history.

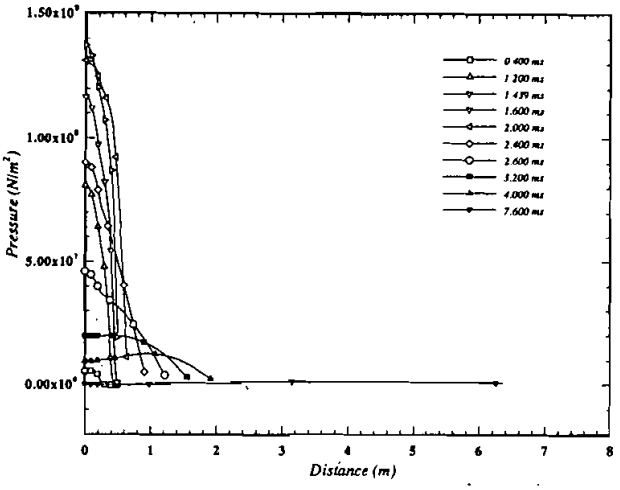

Figure 5. Calculated axial pressure distribution along the radial location $y = 0.5R$.

Figure 5 shows ten calculated axial pressure distributions along the radial location ($y = 0.5R$) at different times. The predictions indicate that the pressure rapidly builds up at the lower parts of the barrel and leads to a large pressure gradient. Because of the dissipative nature of the presently employed power law scheme, the calculated resolutions for some thermodynamic properties such as pressure are rather smeared compared with those using the FCT high-resolution capturing scheme [17].

Figure 6 presents the calculated pressures in terms of contour levels. The pressure front advances radially as well as axially. Radial variations of pressure are more apparent in the beginning of the combustion phase and near the stagnation region behind the backward facing step of the center core igniter. The computed high pressures in the vicinity of the stagnation region are mainly the result of heat released from the black powders loaded in the center core of the igniter. The pressure keeps increasing and spreading out, accompanied by the propagation of the temperature front, and finally reaches the projectile base as more propellants are being ignited. The peak pressure of 1.38×10^8 N m^{-2} is predicted at time $t = 1.6$ ms. The projectile finally cannot withstand the pressure force acting on its base at time $t = 1.439$ ms and starts to move, resulting in a decrease of pressure.

The gas phase temperature distributions are also important in the sequences of combustion processes, since they largely determine if the propellant can be ignited. Figure 7 shows the computed temperatures at the same time and locations as those for the pressure. The predicted salient temperature profiles at the start of flame spreading are mainly due to the penetration of heated gas ejected from the igniter tube.

As seen from the predicted gas velocity vector plots in Figure 8, the flow structure near the breech end is mainly the consequence of an initial primer blast. It results in a radial type of flow pattern except at the domain behind the step of the center core igniter. The peak of the gas velocity profile develops later due to

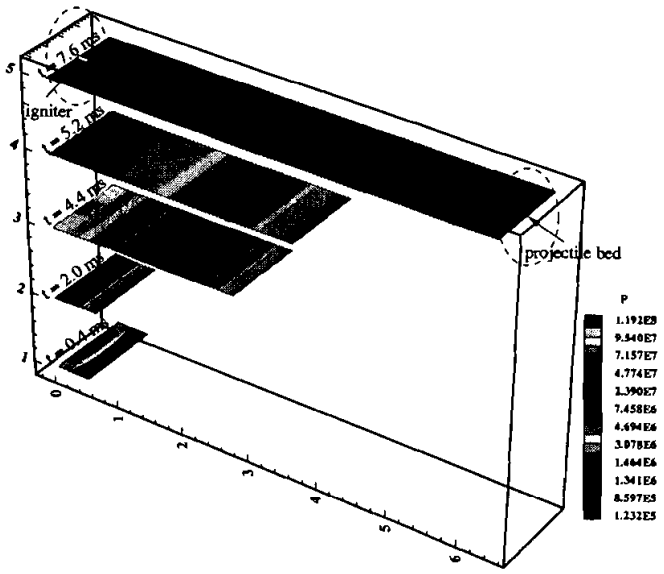

Figure 6. Computed pressure distributions at various times.

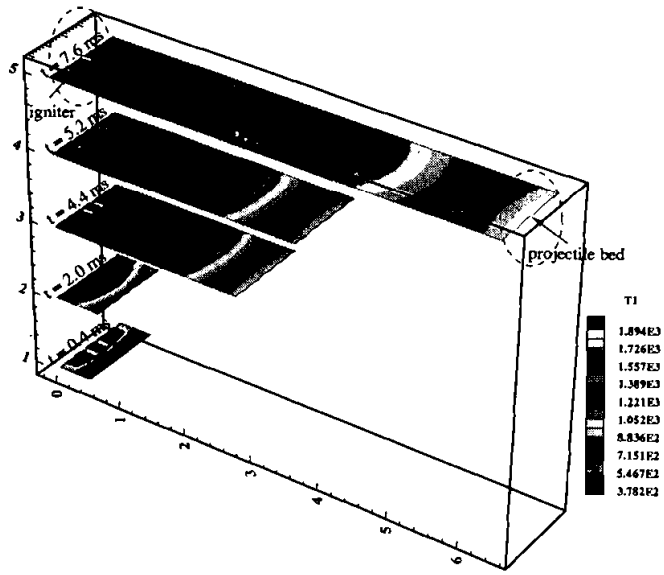

Figure 7. Computed gas phase temperature distributions at various times.

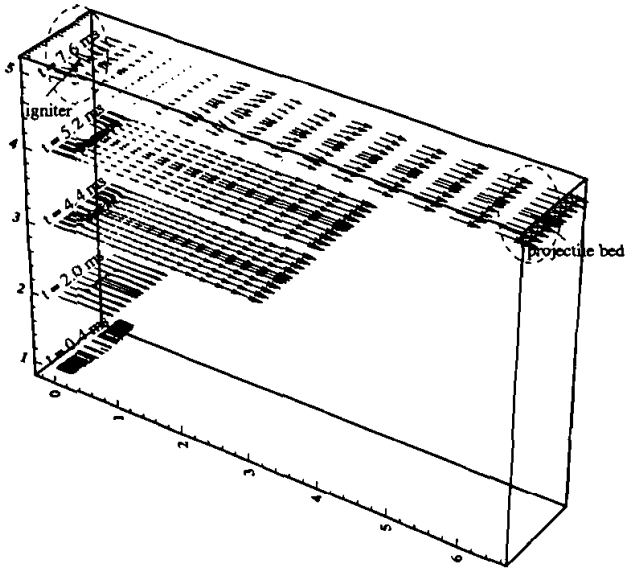

Figure 8. Computed gas velocity vector plots at various times.

the existence of a steep pressure gradient and the flow resistance occurring at the granular bed. Reversed flow appears in the present simulation, which is the result of the strong adverse pressure gradient developed in the granular bed. It may disappear completely in the later ballistic cycle.

Figure 9 depicts the predicted particle velocity profiles at various times. At the start of the ballistic cycle, the particle velocity is comparatively slower than that of the gas velocity due to the inertia of particles and the tight compaction of propellant grains. The sizes of propellants become smaller and fluidized after combustion takes place. These propellant grains will be entrained by the gas motion and therefore move with a faster speed.

Figure 10 presents the axial volume fraction of the solid phase at the radial location $y = 0.5R$. These distributions, computed at 10 different times after the ignition, show that the porosity near the lower end of the barrel decreases fairly rapid. Such reduction in volume fraction is due to the burning of propellants and the forward motion of these particles as they are carried along by the the ejection of hot gas from the center core igniter. After the projectile is propelled, the particle volume fraction drops much more drastically. The tendency toward the uniform volume fraction is caused by the movement of the projectile, which drags the gas with it.

CONCLUSION

We present a mathematical model that can be used to predict two-phase fluid flow and heat and mass transfer in a gun barrel with a mobile projectile. In the modeling of transient two-phase combustion of granular propellants taking place in

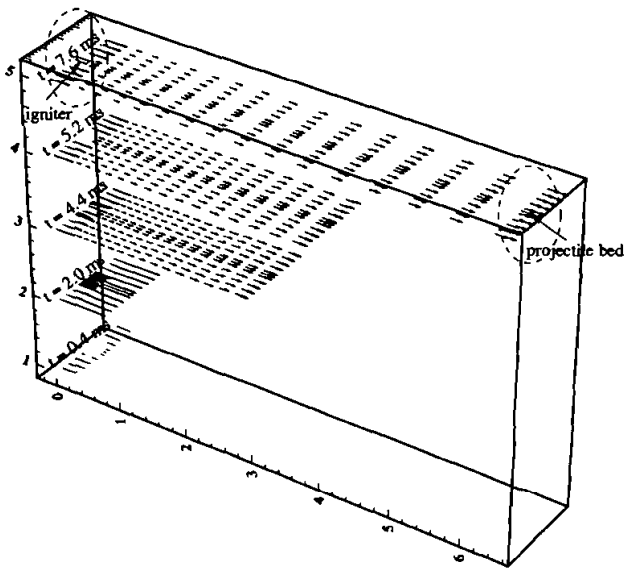

Figure 9. Computed particle velocity vector plots at various times.

the gun's interior ballistics, the framework of the derivation must be formulated in a variable domain, since the location of the projectile base changes almost immediately after firing. We apply the pressure-based compressible computer code, using a semi-implicit stable iteration algorithm, to solve the complete two-phase reactive system of equations.

Results have been presented to illustrate the global nature of combustion processes. Owing to the penetration of ignited gases, the granular propellants near

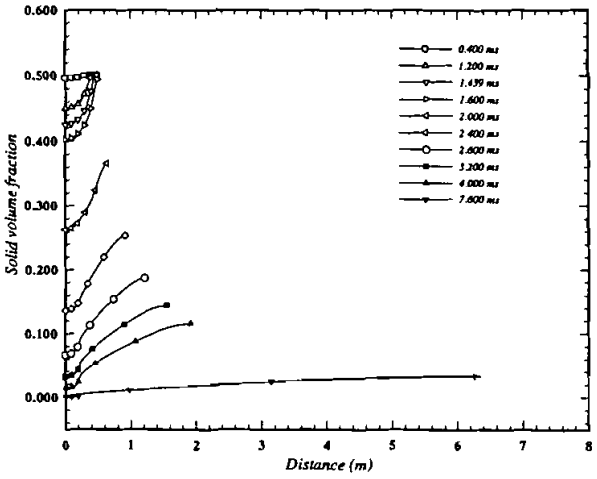

Figure 10. Computed axial volume fraction of solid phase at the radial location $y = 0.5R$.

the breech end were first ignited into the propellant bed. Such combustion products cause a local pressure increase. The pressure wave, together with the flame front, then propagates radially upward to the barrel surface and axially downward to the projectile base. The projectile starts moving as the high-temperature front sweeps through the flow passage and causes more propellants to burn. Then the pressure forces acting on the projectile base exceed the friction force between the gun barrel and the projectile. Figures 3–5 depict the axial distributions of fluid-dynamic and heat transfer variables based on the initial solid loading of 50%. Radial distributions are also presented in contour levels in a two-dimensional time-varying domain. For clearly depicting the kinematic motion of a mobile projectile during the ballistic cycle, the variations in location, velocity, and acceleration are also given for the projectile.

The main conclusions that can be drawn from the present study are as follows.

1. A steep pressure gradient will develop before the projectile being propelled forward. Such increase in pressure is mainly due to the compression wave resulting from the burning of granular propellants. As seen from the presented velocity plots, one can find the reverse gas flow propagating from the downstream portion of the granular bed to the breech end. This flow reversal is mainly the result of pressure reflection from the projectile base, which will be accompanied by the projectile motion but will appear in the subsequent ballistic cycle.
2. As confirmed from the locus of the projectile motion, the peak pressure occurring in the fluidized bed will gradually become uniform as the projectile moves forward.
3. The effect of ejected hot gas emanating from the igniter is seen in Figure 8, illustrating the velocity vector plots. Both the existence of a steep pressure gradient and flow resistance occurring in the granular bed result in the formation of peak gas velocity. A reversed flow pattern may appear under the conditions of a strong adverse pressure gradient in the granular bed.
4. Particle velocity is comparatively slower than gas velocity at the start of the ballistic cycle due to the inertia and compaction of propellant grains. The solid propellants will be continuously fluidized and will be entrained by the gas motion. The particles therefore will move at a faster pace.
5. A much more salient temperature profile has been found at the beginning of flame spreading. The combination of combustion products and the primer gas assists in spreading the flame through the granular bed. The changes in temperature tend to be milder later on, when the projectile moves.
6. The penetrated hot gas emanating from the igniter will be resisted by the interphase drag. It leads to motion and compaction of the solid phase.

REFERENCES

1. K. K. Kuo, *Principals of Combustion*, John Wiley, New York, 1986.
2. W. C. Taylor, J. W. Kelso, M. R. Mayers, and W. W. Blakely, A Graphical System for Interior Ballistic Computation, Ballistic Research Lab., Rept. 825, 1952.

3. P. G. Baer, A Mass Point Computer Program for the Gas Dynamic Problems of High Velocity Gun Interior Ballistic, *Proceedings of 2nd ICRPG/AIAA Solid Propellant Conference*, Anaheim, Calif., 1967.
4. K. K. Kuo, R. Vichnevetsky, and M. Summerfield, Theory of Flame Front Propagation in Porous Propellant Charges under Confinement, *AIAA J.*, vol. 11, pp. 444–451, 1973.
5. K. K. Kuo, J. H. Koo, T. R. Davis, and G. R. Coates, Transient Combustion in Mobile Gas-Permeable Propellant, *Acta Astronaut.*, vol. 3, pp. 573–591, 1976.
6. H. Krier, S. Rajan, and W. F. Van Tassell, Flame Spreading and Combustion in Packed Beds of Propellant Grain, *AIAA J.*, vol. 14, no. 3, pp. 301–309, 1976.
7. P. S. Gough, The Flow of a Compressible Gas through an Aggregate of Mobile Reacting Particle, Ph.D. thesis, Dept. of Mechanical Engineering, McGill University, Oct. 1974.
8. E. B. Fisher and A. P. Trippe, A Mathematical Model of Center Core Ignition in the 175 mm Gun, Calspan Rept. VQ-5163-D-2, March 1974.
9. A. B. Yu, Statistical Hydromechanics of Disperse Systems—1: Physical Background and General Equations, *J. Fluid Mech.*, vol. 49, part 3, pp. 498–507, 1971.
10. S. L. Soo, *Fluid Dynamics of Multiphase Systems*, Blaisdell, Waltham, Mass., 1967.
11. P. S. Gough and F. J. Zwarts, Modeling Heterogeneous Two-Phase Reacting Flow, *AIAA J.*, vol. 17, no. 1, pp. 17–25, 1979.
12. T. B. Anderson and T. Jackson, A Fluid Mechanical Description of Fluidized Bed, *I EC Fundam.*, vol. 6, no. 4, pp. 527–539, 1967.
13. S. Whitaker, The Transport Equations for Multi-Phase Systems, *Chem. Eng. Sci.*, vol. 28, pp. 139–147, 1973.
14. E. B. Fisher and K. W. Graves, Mathematical Model of Double Base Propellant Ignition and Combustion in the 81 mm Mortar, Calspan Rept. GD-3029-D-1, Aug. 1972.
15. P. S. Gough, Numerical Analysis of a Two-Phase Flow with Explicit Internal Boundaries, Naval Ordnance Station, Rept. IHCR 77-5, Indian Head, Md., April 1977.
16. N. C. Markatos, Modeling of Two-Phase Transient Flow and Combustion of Granular Propellants, *Int. J. Multiphase Flow*, vol. 12, no. 6, pp. 913–933, 1986.
17. T. W. H. Sheu, S.-M. Lee, and V. Yang, Analysis of Combustion Processes in Mobile Granular Propellant Bed, *Progr. Astronaut. Aeronaut.*, vol. 154, pp. 477–490, 1993.
18. P. S. Gough, Two-Dimensional Convective Flame Spreading in Packed Beds of Granular Propellant, U.S. Army Armament Research and Development Command Ballistic Research Laboratory Rept. ARBRL-CR-00404, July 1979.
19. H. J. Gibeling, R. C. Buggeln, and H. McDonald, Development of a Two-Dimensional Implicit Interior Ballistics Code, U.S. Army Armament Research and Development Command Ballistic Research Laboratory Rept. ARBRL-CR-00411, Jan. 1980.
20. H. J. Gibeling and H. McDonald, Development of a Two-Dimensional Implicit Interior Ballistics Code, U.S. Army Armament Research and Development Command Ballistic Research Laboratory Rept. ARBRL-CR-00451, March 1981.
21. N. C. Markatos and D. Kirkcaldy, Analysis and Computation of Three-Dimensional Transient Flow and Combustion through Granulated Propellants, *Int. J. Heat Mass Transfer*, vol. 26, no. 7, pp. 1037–1053, 1983.
22. J. Corner, *Theory of the Interior Ballistics of Guns*, John Wiley, New York, 1950.
23. P. K. Sweby, High Resolution Schemes Using Flux Limiters for Hyperbolic Conservation Laws, *SIAM J. Numer. Anal.*, vol. 21, pp. 995–1011, 1984.
24. S. V. Patankar, *Numerical Heat Transfer and Fluid Flow*, 1st ed., Hemisphere, Washington, D. C., 1980.
25. T. W. H. Sheu, S. M. Lee, and J. Y. Lee, Body-Fitted Solution for Transient Compressible Flow at Low Speed, in *Numerical Methods in Laminar and Turbulent Flow*, vol. VII, part I, pp. 1230–1238, Pineridge Press, Swansea, U.K., 1991.
26. Y. P. Yang, Combustion Phenomena inside an Internal Gun Ballistics, Master's thesis, Institute of Mechanical Engineering, Tamkang University, Republic of China, 1992.